17th AIAA/3AF International Space Planes and Hypersonic Systems and Technologies Conference
24 - 28 September 2012, Tours, France

AIAA 2012-5909

Sensitivity of Flight Dynamics of Hypersonic Vehicles to Design Parameters

Derek J. Dalle*, Sean M. Torrez†, James F. Driscoll‡

DOI: 10.2514/6.2012-5909

Dynamic stability is an important concern for air-breathing hypersonic vehicles. Certain design strategies can be used to ensure the stability of the vehicle, such as placing ballast at the nose of the vehicle or increasing the size of the horizontal stabilizers. However, these changes may also increase the drag and thus fuel consumption of the vehicle. To investigate these tradeoffs, this paper uses a trajectory analysis to calculate the sensitivity of both stability parameters and fuel consumption. The most effective parameter to affect the stability is the location of the center of gravity, but other design variables explored include dihedral angle of the horizontal stabilizers and several others. The trajectory used includes both ram-mode and scram-mode flight conditions, and the Mach number at which ram-scram transition occurs is another important consideration. To investigate these sensitivities, a vehicle model called MASTrim designed specifically for flight dynamics applications has been developed. The low-order fundamental model used accounts for complex phenomena such as shock interactions, fuel-air mixing, finite-rate chemistry, and the adjusting shape of the nozzle exhaust plume.

Nomenclature

$\mathbf{A}, \mathbf{B}$	=	linearization matrices
a	=	local speed of sound
C_L	=	lift coefficient
$\mathbf{f}$	=	function for equations of motion
f_{fuel}	=	current fuel divided by max fuel
g	=	9.80665 m/s^2, reference gravity
h	=	geodetic altitude
I	=	specific moment or product of inertia
$\bar{I}_{sp}$	=	rocket-equivalent specific impulse
L	=	geodetic latitude
M	=	Mach number
m	=	vehicle mass
$\dot{m}_f$	=	fuel mass flowrate
n_{ext}	=	number of external inlet ramps
n_{int}	=	number of internal inlet turns
P	=	roll rate
p	=	pressure
Q	=	pitch rate
q	=	dynamic pressure
R	=	yaw rate
$\mathbf{r}$	=	position vector
r_p	=	inlet compression ratio
S	=	reference lifting area of vehicle
t	=	time
u	=	flow velocity in combustor
$\mathbf{u}$	=	vector of control variables
$V, \mathbf{v}$	=	vehicle velocity
x, y, z	=	physical coordinates
$\mathbf{x}$	=	vector of state variables
$\mathbf{Y}$	=	vector of species mass fractions
α	=	angle of attack
β	=	sideslip angle
γ	=	flight path angle
δ	=	deflection angle or control input
θ	=	pitch angle or angle of flow
λ	=	longitude
$\boldsymbol{\xi}$	=	vector of inputs to trim solver
σ	=	velocity heading angle
τ	=	integration variable for time
$\boldsymbol{\nu}$	=	vector of trim variables
ϕ	=	roll angle
ψ	=	yaw angle
$\psi_{horizontal}$	=	elevator dihedral angle
$\boldsymbol{\omega}$	=	angular velocity

Subscripts/superscripts

0	=	trim value or initial value
∞	=	freestream value
b	=	body frame
CE	=	collective (average) elevon value
cg	=	center of gravity
CR	=	collective (average) rudder value
DE	=	differential (left minus right) elevon value
ER	=	equivalence ratio
nb	=	between navigation and body frames
x, y, z	=	axes for inertia tensor values

I. Introduction

Although air-breathing hypersonic vehicles have the potential to dramatically increase fuel efficiency compared to rocket-propelled vehicles, they also introduce many challenges. In addition to the technological challenges, these vehicles also have a tendency to be unstable [1–4]. This is largely because the lift-producing inlet pulls the center of pressure forward, and nozzles shorter than inlets tend to push the center of gravity aft.

The purpose of this work is to investigate how various design parameters affect both stability properties and fuel usage. We use as a starting point a vehicle design that is stable in both the longitudinal short-period mode and the lateral-directional Dutch roll mode. This baseline stable vehicle is called MAX-1 for convenience. Perturbations to this vehicle are considered with the idea of altering the stability properties and performance. A reference trajectory is used that accelerates from Mach 5 to Mach 12 with a constant dynamic pressure of 1 atm and a constant acceleration of 2 m/s^2. Along this trajectory, all the vehicle designs considered in this paper experience ram-to-scram transition. The Mach number at which transition occurs is another aspect of performance that is measured throughout the calculations, but transition appears to have surprisingly little effect on the stability of the vehicle.

The stability analysis is focused on two modes of the linearized flight dynamics. The short-period mode describes a pitching motion of the vehicle. In particular it is a mode that involves the angle of attack, α, and the pitch rate, Q. The second mode considered is a mode that involves the sideslip angle, β, and the yaw rate, Q, and this mode is called the Dutch-roll mode. Both of these modes are standard for air vehicles [5], and their behavior is not significantly different for hypersonic vehicles. Some modes of the linearized flight dynamics for

*Graduate Research Assistant, Department of Aerospace Engineering; dalle@umich.edu. Student Member AIAA

†Postgraduate Research Assistant, Department of Aerospace Engineering; smtorrez@umich.edu. Student Member AIAA.

‡Professor, Department of Aerospace Engineering; jamesfd@umich.edu. Fellow AIAA.

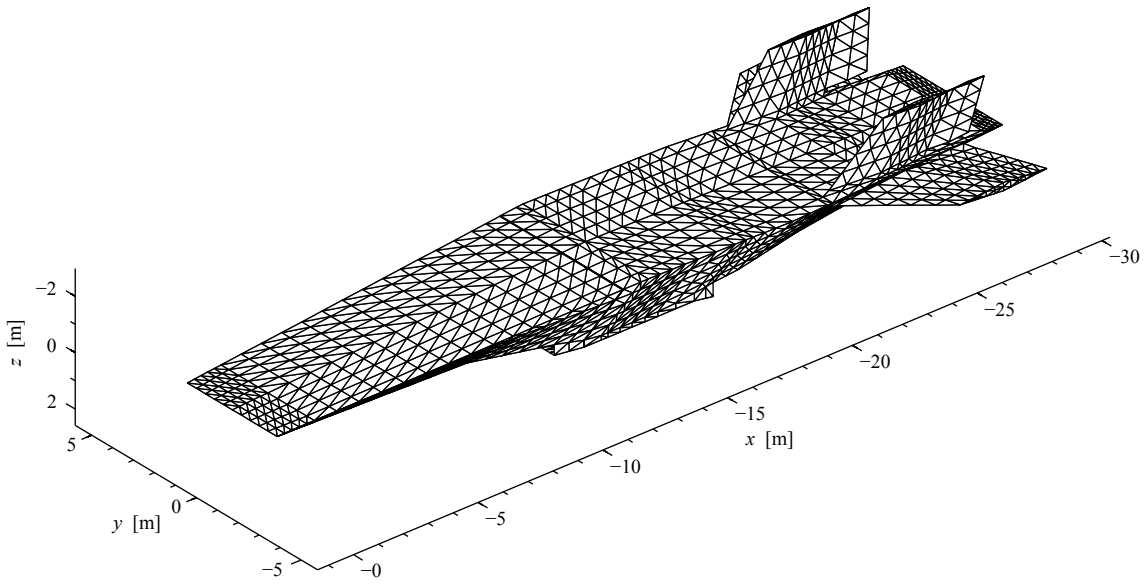

Figure 1. Isometric view of baseline vehicle.

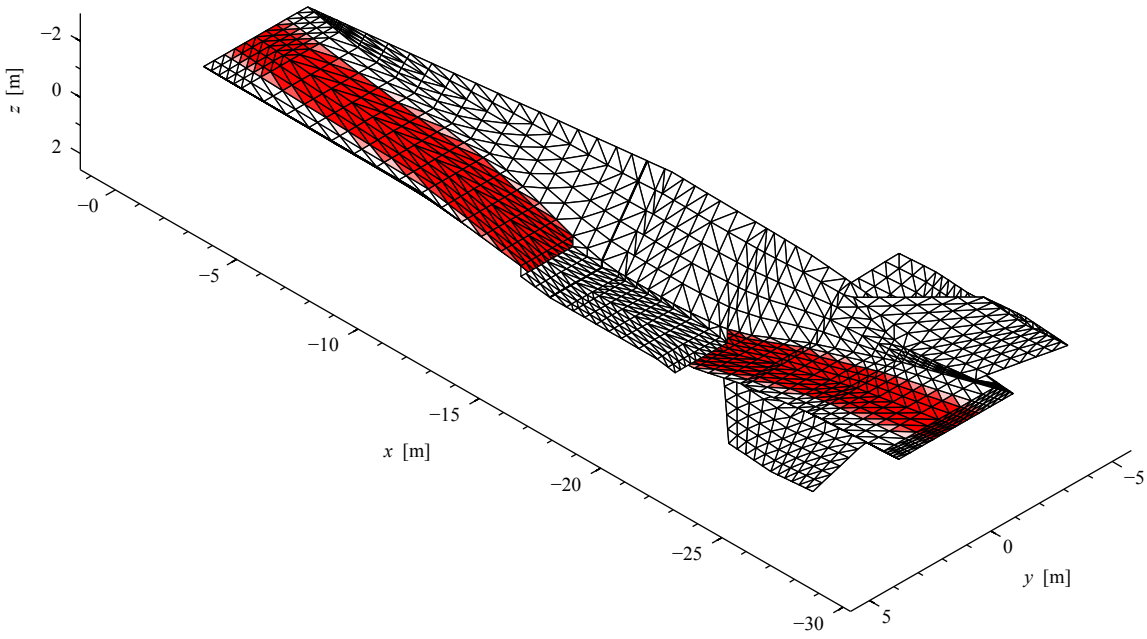

Figure 2. View of baseine vehicle from below with propulsive surfaces shaded.

hypersonic vehicles differ from those of traditional aircraft, such as the combination of the phugoid and altitude modes [1, 6], but the times to double associated with these modes are so long that they are not discussed in this work.

Little has been recorded about the lateral-directional dynamics of hypersonic vehicles. Breitsamter et al. [7] discuss the lateral-directional dynamics of a hypersonic test vehicle and a carrier stage of a two-stage transportation system. They also investigate a coupling between the roll and spiral modes, which is called lateral phugoid. Choi [8] also discussed lateral dynamics and handling properties using a simplified model. Previous work by the authors [4, 6] has also investigated lateral-directional dynamics in a limited capacity. This complements may studies of longitudinal dynamics [1–3]. Dickeson et al. [9, 10] discuss factors that affect sizing of the longitudinal control surfaces; the present work seeks to do the same for lateral-directional properties.

The vehicle model used for this work is the Michigan/AFRL Scramjet Trim (MASTrim) code, which has been described in several previous papers [11–13]. MASTrim consists primarily of an engine model called MASIV (Michigan/AFRL Scramjet In Vehicle) with a simple external aerodynamics model; rotating, ellipsoidal-Earth equations of motion; and tools for trim and stability analysis. As a whole, MASTrim is a collection of low-order models that can model such effects as shock interactions, fuel-air mixing, and finite-rate chemistry but can also calculate the forces on a vehicle in about 5 seconds using a single processor with clock speed in the neighborhood of 2.6 GHz.

In addition to a summary of the vehicle and vehicle model in Sec. II, the paper includes a discussion of the equations of motion, the trim process, and a description of the reference trajectory in Sec. III. The results include plots of the short-period and Dutch-roll modes for multiple vehicles throughout the reference trajectory, and the trim variables throughout the trajectory are also provided to explain the differences in stability.

II. Vehicle Model

The baseline vehicle used for this work are very similar to a scaled up X-43 vehicle. The baseline vehicle, called MAX-1, is shown in Figs. 1 and 2. In Fig. 2 the shaded triangles show the surfaces that are analyzed by the engine model, while the remaining surfaces are analyzed by the external aerodynamics model. Standard body-fixed coordinates are used for the vehicle: the x-axis points forward, the y-axis points to the right of the vehicle, and the z-axis points downward.

The MASTrim vehicle model is split into several sections that interact with each other. The vehicle is split into engine and non-engine components, with the engine being split further into inlet, isolator, combustor, and nozzle models. The rest of the MASTrim model is a simple exterior aerodynamics model and a program to compute the equations of motion. Figure 3 shows how information is passed among these components with distinct appearances for inputs (white boxes with square corners), vehicle submodels (gray boxes), and auxiliary models (dark boxes with white text).

The MASTrim model is capable of constructing and analyzing a range of "X-43-like" vehicles that are based on a set of about 50 design parameters. The vehicle used here has a length of 28.5 m and is designed for Mach numbers ranging from Mach 7 to Mach 11. The horizontal width of the engine is 2.14 m while the nose width is 4.29 m, and the maximum vehicle width is 6.00 m. The maximum vertical width of the vehicle (not counting the tails) is 2.79 m. The fuel is hydrogen for all simulations.

The subsections explain the design and analysis of each component. The vehicle design is not the result of a formal multi-disciplinary design optimization, but each component has been selected according to certain design principles. For example, the changing shock positions that result from changing Mach number and angle of attack have a significant impact on the inlet performance, and the design has been chosen explicitly to have acceptable performance for a range of Mach numbers and angles of attack [14, 15]. Each subsection also explains the links among the various models as shown in Fig. 3 in more detail.

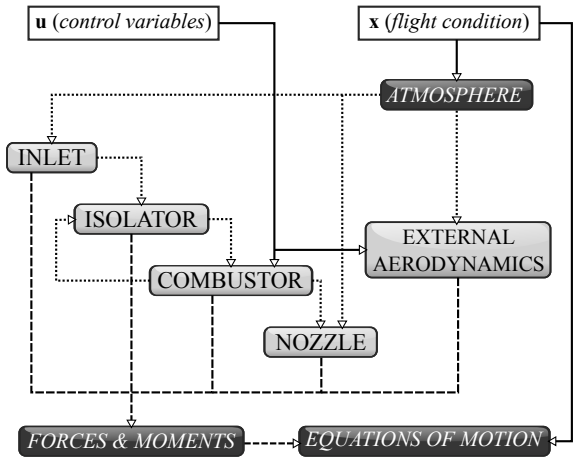

Figure 3. Overview of information flow within MASTrim. The white boxes show inputs, the gray boxes show core vehicle models, and the dark boxes show auxiliary models. Solid lines represent information directly from the inputs, dashed lines show forces and moments, and dotted lines represent thermodynamic state information.

A. Inlet and Nozzle Model

The inlet and nozzle have two-dimensional designs, and they are analyzed using a two-dimensional model called SAMURI (Supersonic Aerodynamic Method Using Riemann Interactions). In [11], we compared the static pressure profile and stagnation pressure loss for a sample inlet design with the results of 2D CFD (computational fluid dynamics) and a 3D experiment and found the results to be agree to within 6% consistently.

Instead of modeling the velocities and thermodynamic properties of the inlet flow on a grid, the SAMURI model tracks the waves that determine a two-dimensional supersonic flow. The properties of each wave can be calculated using simple oblique shock analysis [16] or a discretized form of Prandtl-Meyer expansion theory [13]. Leading edges and other vertices of the inlet geometry each introduce at least one wave, and each wave can interact with the surface of the inlet or other waves. When two or more waves interact, the result is a Riemann problem as described in [13].

Although the user does not generate a grid for this model, the waves determine the "grid" on the flow solution. Each cell has boundaries that are either shock waves, discretized expansion waves, slip discontinuities, the surface of the vehicle, or the edge of the solution domain. Furthermore, each cell has constant properties such as density, pressure, temperature, flow speed, and flow direction.

Figure 4 shows contour plots of the static temperature solution for the MAX-1 vehicle at a particular trimmed flight condition. Figures 4a and 4b show the inlet solution while Figs. 4c and 4d show the nozzle solution.

The MAX-1 inlet shown here is designed for Mach numbers between 7 and 11 and angles of attack between $-0.5°$ and $+1°$. The angles of the external ramps are $4.7°$ and $11.9°$. At Mach 8, this means that there is a substantial amount of spillage, which can be seen from the fact that the shock in the lower left corner of Fig. 4b is some distance away from the cowl leading edge. Furthermore, the shock that originates at the cowl leading edge hits the inlet body downstream of the body vertex that is often called a "shoulder." At the highest design Mach number, 11, this shock would hit the body just upstream of the next body vertex downstream (or second "shoulder"). The approach to design inlets for a range of flight conditions is described in [14] and [15], and it differs from the traditional idea of optimizing performance at a single flight condition [17]. The design process mostly consists of making sure that the inlet shocks do not have detrimental interactions when the vehicle is flying within the specified range of flight conditions. However, this does not necessarily imply that performance is always poor outside the design range. Furthermore, a wider range of design Mach numbers tends to reduce peak performance [14],

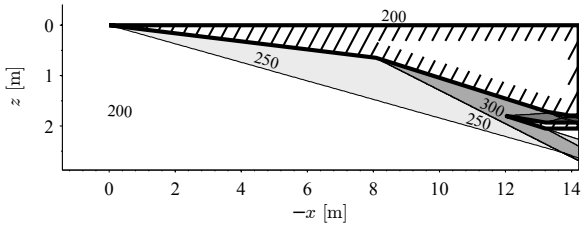

a) Inlet.

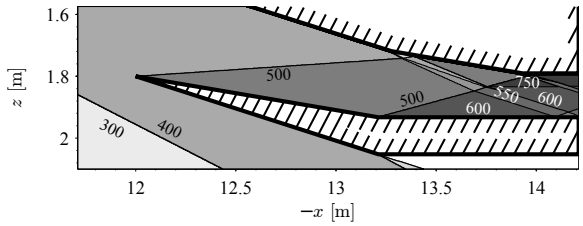

b) Inlet cowl region.

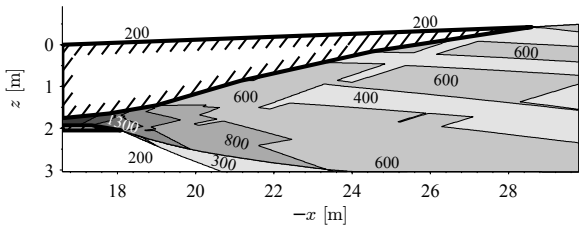

c) Nozzle.

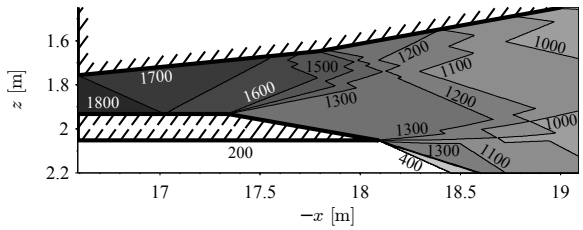

d) Nozzle cowl region.

Figure 4. Some sample inlet and nozzle solutions at a trimmed Mach 8 flight condition. All values are temperature in Kelvins. The nozzle results lack the expected smoothness due to the discrete model of each expansion fan.

so there is a design tradeoff that leads design Mach number to be a particularly interesting design parameter.

B. Combustor/Isolator Model

The combustor model is a quasi-one-dimensional model, but fuel-air mixing and heat release are modeled as three-dimensional processes [12]. That is, the fuel is injected from the wall as a three-dimensional jet in a cross flow, and the local fuel mixture fraction profiles are determined from measured scaling relations. At each (x, y, z) location, the fuel mixture fraction is converted into a chemical reaction rate using turbulent mixing and combustion lookup table. The reaction rates are integrated into the one-dimensional fluid flow conservation equations, which are ordinary differential equations for the thermodynamic states, density, pressure, temperature, flow velocity, and the mass fractions $\mathbf{Y}$. The reaction rates, $\dot{\mathbf{Y}}$, are a function of all three spatial coordinates given by

$$\frac{\mathrm{d}\mathbf{Y}}{\mathrm{d}x} = \frac{1}{u}\dot{\mathbf{Y}}(x) = \frac{1}{u}\iint \dot{\mathbf{Y}}(x, y, z)\,\mathrm{d}y\,\mathrm{d}z \tag{1}$$

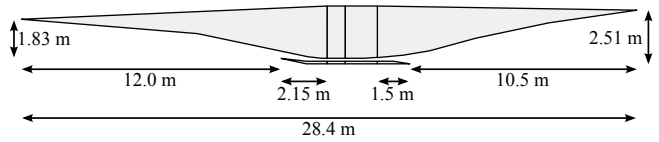

a) Geometry of the full flowpath.

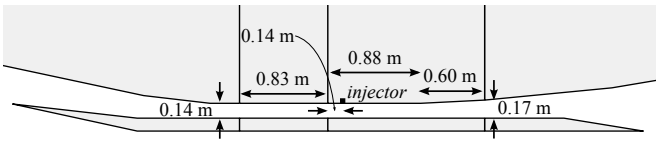

b) Geometry of the internal flowpath.

Figure 5. Schematic of engine flowpath. The vertical lines mark the separation between the inlet, isolator, combustor, and nozzle. The engine width is 2.14 m.

More details on both the thermodynamic equations and the finite-rate chemistry model can be found in [12].

When the vehicle is operating in full scram mode, the isolator does not establish a shock train, and the solution steps directly from inlet to isolator to combustor to nozzle without any feedback from the downstream components. However, when the vehicle goes into ram mode, and the isolator and combustor are coupled and must be solved simultaneously. The isolator slows the flow to subsonic speeds (with respect to the vehicle), and the flow becomes supersonic again at some point in the combustor. The engine code contains a submodel that determines the correct isolator strength that causes the subsonic-to-supersonic transition in the combustor to satisfy certain conditions [18, 19].

The engine flowpath geometry is shown in Fig. 5. The combustor geometry consists of a constant-area section followed by another section with a 4° divergence angle, and the width of the vehicle is a constant 2.14 m. Hydrogen fuel is injected from a row of injectors that are located at a single x-coordinate 0.14 m downstream of the start of the combustor, and the injectors are only on one side of the combustor duct. Each injector has a diameter of 3.45 cm, and they are spaced so that there are $N = 14$ injector ports per meter in the y-direction.

C. External Aerodynamics Model

To calculate the forces on the vehicle's exterior, as shown in Figs. 1 and 2, we use a modification of the panel method from [20] that also incorporates a model for viscous forces. A triangular surface mesh is applied to the vehicle, the freestream velocity is projected onto the surface, and the angle between the freestream and the projected velocity is then used to compute the thermodynamic properties behind either an oblique shock or a Prandtl-Meyer expansion, depending on the sign of the angle. This method is similar in nature to Newtonian impact theory [2] and piston theory [21] in that the pressure is calculated independently for each triangular panel. This method was shown to agree with the HABP (Hypersonic Arbitrary Body Program) to within a few percent, especially for small angles of attack [20].

The flow also accounts for the angular velocity of the vehicle, $\boldsymbol{\omega}^b_{nb}$, so that the "freestream" velocity for a given triangle is

$$\mathbf{v}^b = \mathbf{v}^b_\infty + \boldsymbol{\omega}^b_{nb} \times (\mathbf{r}^b - \mathbf{r}^b_{cg}) \tag{2}$$

where the superscript b means that each vector is written in the body coordinate frame described earlier. Then the deflection angle is calculated by solving

$$\sin\delta = -\frac{\hat{\mathbf{n}}^b \cdot \mathbf{v}^b}{\|\mathbf{v}^b\|} \tag{3}$$

The pressure on the triangle is given by usual oblique shock theory [16] using $M = \|\mathbf{v}^b\|/a_\infty$ as the Mach number and δ as the deflection angle when δ is positive and Prandtl–Meyer theory when $\delta < 0$.

The dependence on angular velocity is important because the sensitivity of the forces and moments to the angular velocity are part of the calculation of the linearized dynamics. If these sensitivities were

assumed to be zero, there would be no proper short-period or Dutch-roll modes.

Boundary layer thickness and friction coefficient are computed using the Van Driest II method [22]. Considering the boundary layer to restart on each triangle would lead to a considerable overestimate of viscous drag, and to account for this, a momentum thickness is calculated for each edge of each triangle. For each edge that is part of a leading edge, this thickness is set to zero. For each surface, the momentum thickness at the upstream edge(s) is used to calculate the momentum thickness at the downstream edge(s), which is then passed on to the next surface. This model provides a first estimate of the viscous drag on the exterior of the vehicle, but it does not account for shock-boundary layer interactions. The boundary layer is assumed to be turbulent on the entire surface of the vehicle.

D. Mass Properties

To provide a first estimate of the mass properties of a hypersonic vehicle, correlations provided by Chudoba [23] are used. These correlations give estimated weights for the vehicle and how much fuel it can carry, and the correlations are dependent on the planform area of the vehicle, design Mach number, and fuel type.

Once the mass of the vehicle is calculated, an inertia tensor must be constructed. For this model, we assume that the mass is distributed evenly throughout the vehicle except for some ballast placed at the nose to shift the center of mass forward. This assumption is used regardless of how much fuel is currently in the vehicle, and as a result, the inertia tensor divided by mass is constant. Table 1 lists the mass properties of the vehicle used for this paper.

The center of mass of this vehicle is forward of the center of volume by 5% of the vehicle length, which means that the center of mass is located at 56% of the vehicle's total length. Ballast can improve the stability, but it can negatively affect the elevator setting required for trim, which can increase the drag. For X-43-like vehicles, extra mass in the nose can also improve the trim condition because it counteracts the strong nose-up moment that the geometry naturally produces.

Table 1. Mass properties of vehicle.

Symbol	Name	Value
	operational empty mass	1.50×10^4 kg
	maximum fuel mass	2.33×10^4 kg
I_{xx}	specific moment of inertia	2.32 m^2
I_{yy}	specific moment of inertia	34.30 m^2
I_{zz}	specific moment of inertia	35.99 m^2
I_{xz}	specific product of inertia	0.53 m^2
x_{cg}	center of mass location	−12.55 m
z_{cg}	center of mass location	0.16 m

III. Equations of Motion

For hypersonic vehicles, the velocities and altitude are high enough that the assumption of a flat Earth is no longer valid. As a result, we implement the equations of motion for a rotating ellipsoidal Earth based on a WGS84 shape and gravity model.

The output of the MASTrim hypersonic vehicle model is an acceleration and an angular acceleration in the body frame, which is written as

$$\dot{\mathbf{x}} = \mathbf{f}(\mathbf{x}, \mathbf{u}) \tag{4}$$

Here $\mathbf{x}$ is a vector of state variables, and $\mathbf{u}$ is a vector of control variables. Although MASTrim has been written using general rigid-body six-degree-of-freedom equations of motion, the flight conditions in this paper are all for equatorial flight directly eastward.

A. Trim

Given a target acceleration $\dot{\mathbf{x}}$, finding a trimmed flight condition becomes a problem of finding values of $\mathbf{x}$ and $\mathbf{u}$ such that Eq. (4) is satisfied. Typically, we define $\mathbf{x} \in \mathbb{R}^n$ and $\mathbf{u} \in \mathbb{R}^m$. Since we consider the equations to be all first-order differential equations, $\mathbf{x}$ has 12 components. If $\mathbf{u}$ has m components, the trim problem is a system of 12 equations and $12 + m$ variables. It is assumed that the position, velocity, and angular velocity are independently specified. For example, to find a trimmed flight condition at a given velocity and altitude, V and h are determined before the trim analysis is computed. This reduces the problem to 6 equations and $2 + m$ variables. In our case,

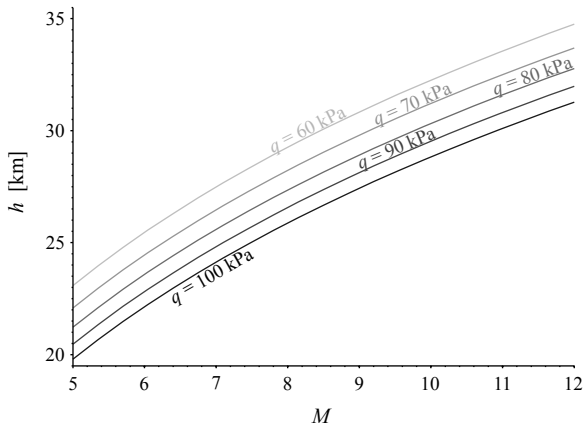

Figure 6. Contours of dynamic pressure as a function of Mach number and altitude. The non-grayed portion is the flight corridor used in this paper.

$$\mathbf{u} = \begin{bmatrix} \delta_{ER} & \delta_{CE} & \delta_{DE} & \delta_{CR} \end{bmatrix}^T \tag{5}$$

so $m = 4$. It is convenient to write the trim equations

$$\dot{\mathbf{x}} = \mathbf{f}(\boldsymbol{\xi}, \boldsymbol{\upsilon}) \tag{6}$$

where

$$\boldsymbol{\xi} = \begin{bmatrix} L & \lambda & h & V & \beta & \gamma & \sigma & P & Q & R \end{bmatrix}^T \tag{7}$$

is considered a vector of "fixed" parameters. The independent variables that must be solved for are

$$\boldsymbol{\upsilon} = \begin{bmatrix} \alpha & \phi & \delta_{ER} & \delta_{CE} & \delta_{DE} & \delta_{CR} \end{bmatrix}^T \tag{8}$$

where δ_{CE} is the average of the left and right elevator deflection angles (defined so that a positive deflection moves the trailing edge down) and δ_{DE} is the deflection angle of the right elevator minus the deflection angle of the left elevator.

Evaluating the function $\mathbf{f}$ is relatively expensive because it requires calculating the forces and moments on the vehicle, which in turn requires simulating each shock interaction, the fuel-air mixing, etc. As a result, we want to use a method to solve the trim equations that requires as few evaluations of $\mathbf{f}$ as possible. We use Broyden's method [24], which requires seven function evaluations to calculate the first estimate of the gradient matrix, $\partial\mathbf{f}/\partial\boldsymbol{\upsilon}$, but subsequent estimates are obtained using only the previous estimate of the gradient and the function evaluation of the current iteration.

B. Ascending Trajectory

This paper considers trajectories with constant dynamic pressure. Using an assumed atmospheric model [25], the restriction of flying a constant dynamic pressure trajectory allows us to determine altitude as a function of velocity so that there is a function $h = h(V)$. Differentiating this function with respect to time gives

$$\dot{h} = \frac{\mathrm{d}h}{\mathrm{d}V}\dot{V} \tag{9}$$

Since $\dot{h} = V \sin\gamma$, we can solve for the acceleration,

$$\dot{V} = V\frac{\mathrm{d}V}{\mathrm{d}h}\sin\gamma \tag{10}$$

The dynamic pressure is $q = \frac{1}{2}\rho V^2$ where ρ is given as a function of altitude, $\rho(h)$. Differentiating both sides with respect to altitude gives, for $\dot{q} = 0$,

$$\frac{\mathrm{d}V}{\mathrm{d}h} = -\frac{V}{2\rho}\frac{\mathrm{d}\rho}{\mathrm{d}h}$$

Substituting this result back into (10) gives

$$\dot{V} = -\frac{V^2}{2\rho}\frac{\mathrm{d}\rho}{\mathrm{d}h}\sin\gamma \tag{11}$$

This means that the flight path angle, γ, can be determined from the acceleration, $\dot{V}$.

The dynamic pressures as a function of altitude and Mach number are shown in Fig. 6. We consider the normal operating range of dynamic pressures to be between 60 kPa and one atmosphere (101.325 kPa). Within this range, the highest dynamic pressure results in the best performance. Although drag and thrust are both approximately proportional to dynamic pressure, flying at a lower dynamic pressure, and hence higher altitude, means that a higher angle of attack is required, which increases the drag coefficient. Furthermore, since the net thrust is proportional to dynamic pressure, the same thrust coefficient results in a higher acceleration. As a result, the vehicle tends to prefer the highest dynamic pressure that structural and thermal constraints allow.

C. Fuel Consumption

An appropriate objective for optimizing a trajectory that must connect two fixed flight conditions is the total fuel usage. Although this paper does not discuss trajectory optimization, the total fuel consumption along a trajectory and its sensitivity to vehicle design parameters is worth calculating. The total fuel used along a trajectory is defined as

$$m_f(t) = \int_0^t \dot{m}_f\left(V(\tau), \dot{V}(\tau)\right)\,\mathrm{d}\tau \tag{12}$$

Suppose that a given trajectory is parametrized by n pairs of flight conditions $(V_1, \dot{V}_1), \ldots, (V_n, \dot{V}_n)$. Using trapezoidal numerical integration, we can estimate the fuel used along segment i of the trajectory as

$$\Delta m_{f,i} = \frac{1}{2}\Delta t_i(\dot{m}_{f,i+1} + \dot{m}_{f,i}) \tag{13}$$

A good approximation is still needed for the time spent on segment i. This is somewhat complicated because the two variables, V and $\dot{V}$, are related to each other by a time derivative. However, since only constant-acceleration trajectories are considered here, the time intervals can be written

$$\Delta t_i = \frac{V_{i+1} - V_i}{\dot{V}_i} \tag{14}$$

D. Linearized Flight Dynamics

For this analysis, the equations of motion were linearized about the acceleration condition. Expanding the equations of motion using a first-order Taylor series about a reference condition $\mathbf{x}_0$, $\mathbf{u}_0$ leads to

$$\dot{\mathbf{x}}_0 + \Delta\dot{\mathbf{x}} = \mathbf{f}(\mathbf{x}_0, \mathbf{u}_0) + \left.\frac{\partial \mathbf{f}}{\partial \mathbf{x}}\right|_{\mathbf{x}_0,\mathbf{u}_0}\Delta\mathbf{x} + \left.\frac{\partial \mathbf{f}}{\partial \mathbf{u}}\right|_{\mathbf{x}_0,\mathbf{u}_0}\Delta\mathbf{u}$$

Recognizing that $\dot{\mathbf{x}}_0 = \mathbf{f}(\mathbf{x}_0, \mathbf{u}_0)$, the linearized equations of motion become

$$\Delta\dot{\mathbf{x}} = \mathbf{A}\Delta\mathbf{x} + \mathbf{B}\Delta\mathbf{u} \tag{15}$$

where

$$\mathbf{A} = \left.\frac{\partial \mathbf{f}}{\partial \mathbf{x}}\right|_{\mathbf{x}_0,\mathbf{u}_0} \qquad \mathbf{B} = \left.\frac{\partial \mathbf{f}}{\partial \mathbf{u}}\right|_{\mathbf{x}_0,\mathbf{u}_0} \tag{16}$$

For this analysis we used

$$\mathbf{x} = \begin{bmatrix} V & \alpha & \beta & P & Q & R & \phi & \theta & \psi & h \end{bmatrix}^T \tag{17}$$

and the poles are the eigenvalues of $\mathbf{A}$ using these definitions. The poles are associated with a particular dynamic mode using a modal participation analysis [26]. The most important modes in terms of the vehicle stability and design are the short-period and Dutch-roll modes.

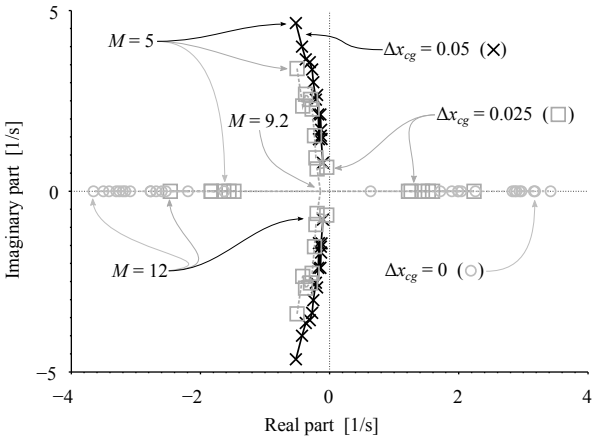

a) Short-period modes.

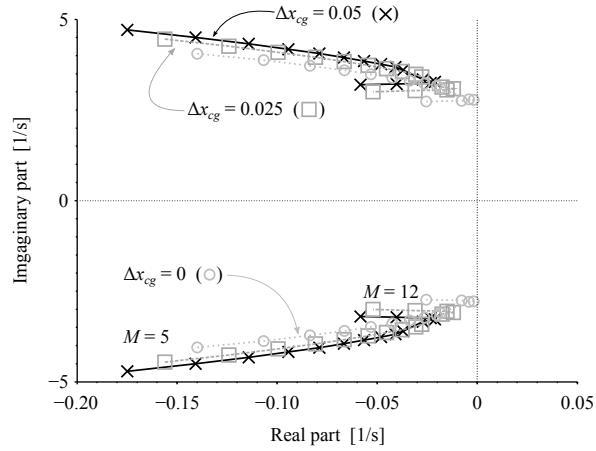

b) Dutch-roll modes.

Figure 7. Plot of poles of linearized dynamics for MAX-1 (Δx_{cg}=0.05) and otherwise identical vehicles with half (Δx_{cg}=0.025) the center-of-gravity shift and no shift (Δx_{cg}= 0).

IV. Results

The results are split broadly into two parts. Sections IV.A-E focus on the effect on the poles of the short-period and Dutch-roll modes from changing one design variable at a time. The five design variables selected are location of center of gravity, change in mass (as fuel is consumed), dihedral angle, design Mach number, and inlet compression ratio. Throughout that discussion, several plots of trim parameters are used to explain the differences in the linearized dynamics. The remaining subsection, Sec. IV.G, discusses how the changes in the design affect performance. Of particular interest is how a stabilizing or destabilizing change to the design affects the fuel consumption.

All results are shown for a trajectory accelerating from Mach 5 to Mach 12 along a velocity-altitude path with a constant dynamic pressure of 1 atm. The acceleration is held constant at 2 m/s^2.

A. Center of Gravity

Moving the center of gravity is the most obvious way to affect the stability of an air vehicle. In this section, the position of the center of gravity is changed without any change in the mass or other properties of the vehicle. The usual method to move the center of gravity for a real vehicle is to add ballast mass at the nose of the vehicle, but changes in mass and shifting the center of gravity are isolated as separate variables in this work.

Figure 7 shows the poles of the linearized open-loop dynamics. The baseline MAX-1 vehicle has a center of gravity that is shifted forward of the center of volume by 5% of the length of the vehicle. Not

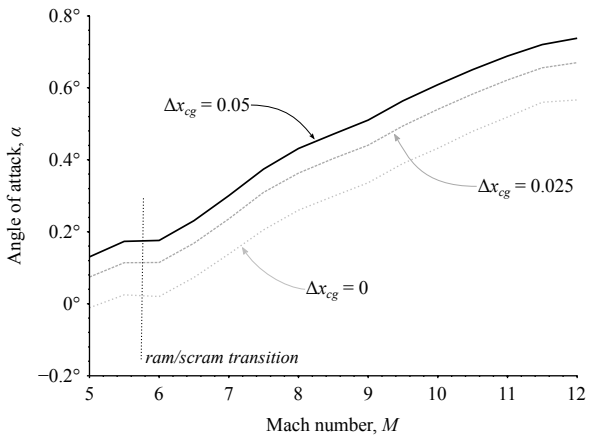

a) Angle of attack (α)

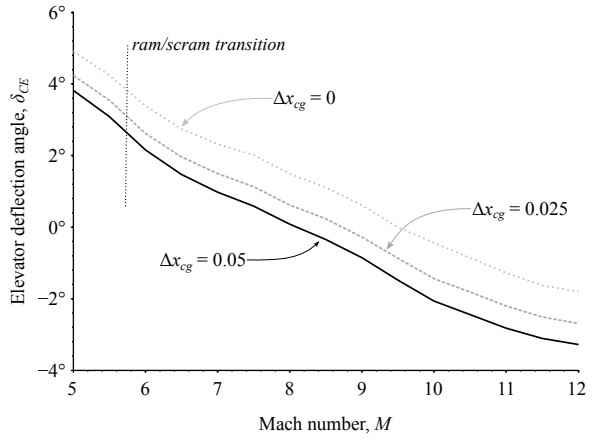

b) Elevator deflection angle (δ_{CE})

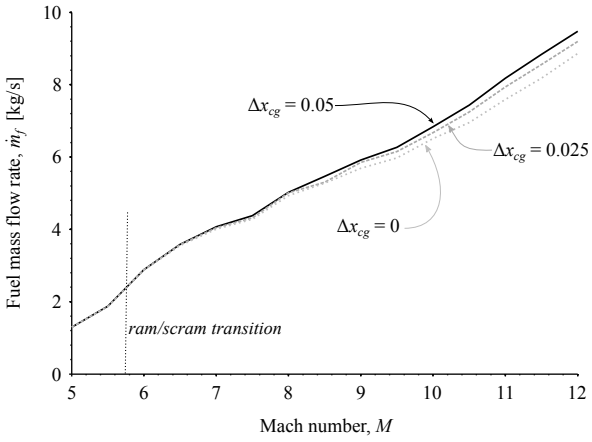

c) Fuel mass flow rate ($\dot{m}_f$)

Figure 8. Plot of state and control variables for MAX-1 (Δx_{cg}= 0.05) and otherwise identical vehicles with half (Δx_{cg}= 0.025) the center-of-gravity shift and no shift (Δx_{cg}= 0).

surprisingly, removing this center-of-gravity offset is destabilizing. For the short-period modes shown in Fig. 7a, the vehicle is stable for all Mach numbers for MAX-1 (Δx_{cg} = 0.05) and unstable for all Mach numbers for the vehicle whose center of gravity is located at the center of volume (Δx_{cg} = 0). For a vehicle with a shift halfway in between these two vehicles (Δx_{cg} = 0.025), the short-period mode transitions from stable to unstable between Mach 9 and Mach 9.5.

The Dutch-roll poles, shown in Fig. 7b, are stable and oscillatory for all three vehicles and all flight conditions on the trajectory. The vehicles with less forward shift have longer times to half and a slightly longer oscillation period. Interestingly, all of the vehicle designs in this work show an abrupt change in the trend of the Dutch-roll modes at Mach 11.

The effects of the center of gravity location on the trim variables are shown in Fig. 8. The location of the center of gravity has a significant effect on both the trim angle of attack and the elevator deflection angle. Both effects are primarily due to the changing net moment caused by moving the center of gravity because both the mass and the surface of the vehicle are unchanged between the two designs. When the center of gravity is farther back, the elevators need to exert a greater moment to counteract the nose-up moment on the vehicle, and thus an increase in the deflection angle is required, as shown in Fig. 8b. Note that a positive deflection angle moves the trailing edge down, which creates a negative (nose-down) pitching moment. The fact that the lever arm of the elevators is reduced by moving the center of gravity closer also helps exaggerate the differences in the deflection angle.

Changes in the trim angle of attack occur because of a need to reduce or increase the nose-up moment resulting from the inlet. Moving the center of gravity aft causes an increase in the nose-up moment resulting from the inlet simply because the length of the lever arm increases. Although this can be counteracted by increasing the elevator deflection, decreasing the angle of attack also decreases the nose-up moment. Which combination of these two actions actually is used depends on also keeping the acceleration at the specified level and balancing lift and weight.

Figure 8c shows that the fuel usage is only slightly affected by the location of the center of gravity. Apparently the combination of decrease in angle of attack and increase in the elevator deflection angle is such that the drag stays about the same. However, at the higher Mach numbers, the fuel mass flow rate decreases slightly as the center of gravity moves backward. This indicates that moving the center of mass forward can increase the total fuel consumption even without accounting for the mass of the ballast.

B. Change in Mass

The baseline specification for MAX-1, which is the vehicle shown in Fig. 1, has its fuel tanks half full (f_{fuel} = 0.5). Therefore a simple way to change the mass of the vehicle is to add or remove some of the fuel. In the MASTrim model, the fuel mass is considered to be distributed evenly throughout the vehicle so that the center of gravity position remains fixed and the inertia tensor scales linearly with the mass.

Figure 9 shows that the additional mass tends to destabilize the vehicle. However, none of the modes goes unstable, and the difference in mass (2300 kg) is quite large. The first result of increasing the mass is to increase the trim angle of attack. If the weight increases without changing the dynamic pressure, a larger lift coefficient is needed in order to satisfy

$$mg \approx C_L q S$$

where S is the reference lifting area of the vehicle. An increase in angle of attack tends to affect the inlet more than other parts of the vehicle, and as a result, increasing the angle of attack tends to be destabilizing. For any air vehicle, an increase in the lift coefficient tends to increase the drag coefficient as well. As a result, this is a case where a destabilizing change also increases the fuel usage.

C. Dihedral Angle

Although the MAX-1 vehicle does not have much wing area, the dihedral angle of the horizontal stabilizers and elevators can affect the lateral-directional stability. The MAX-1 vehicle has a dihedral angle of $\psi_{horizontal}$ = 2.86° (or $\psi_{horizontal}$ = 0.05 radians), and the results were compared to a vehicle with twice the dihedral angle ($\psi_{horizontal}$ = 5.73° or $\psi_{horizontal}$ = 0.1 radians) and a vehicle with the opposite (anhedral) angle ($\psi_{horizontal}$ = −0.05). As shown in Fig. 10b, increasing the dihedral angle makes the Dutch-roll mode more stable for each flight condition in the trajectory, while the short-period mode is mostly unaffected. The slanted sides of the vehicle keep the Dutch-roll mode stable even

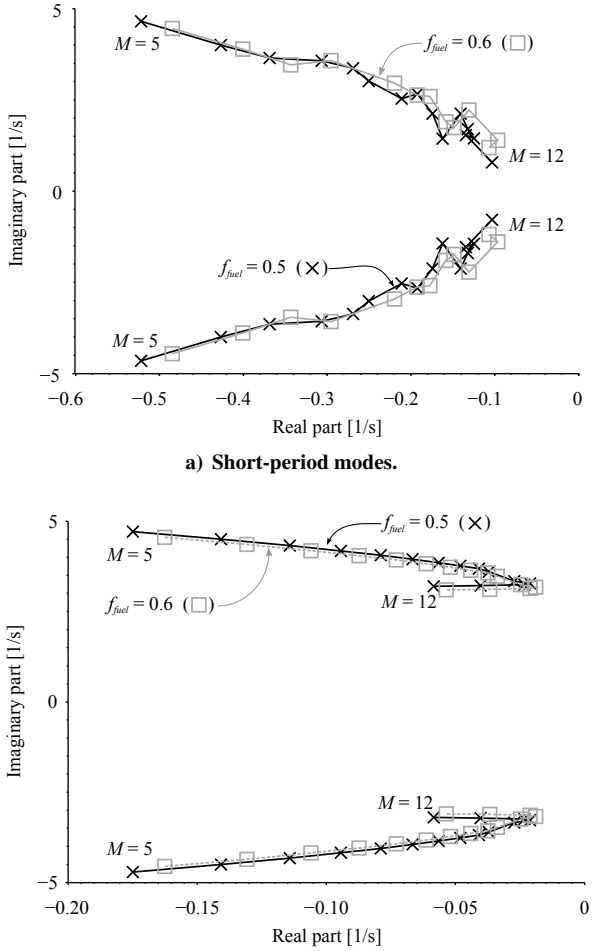

a) Short-period modes.

b) Dutch-roll modes.

Figure 9. Plot of poles of linearized dynamics for MAX-1 (f_{fuel} = 0.5) and an otherwise identical vehicle with more fuel on board (f_{fuel} = 0.6).

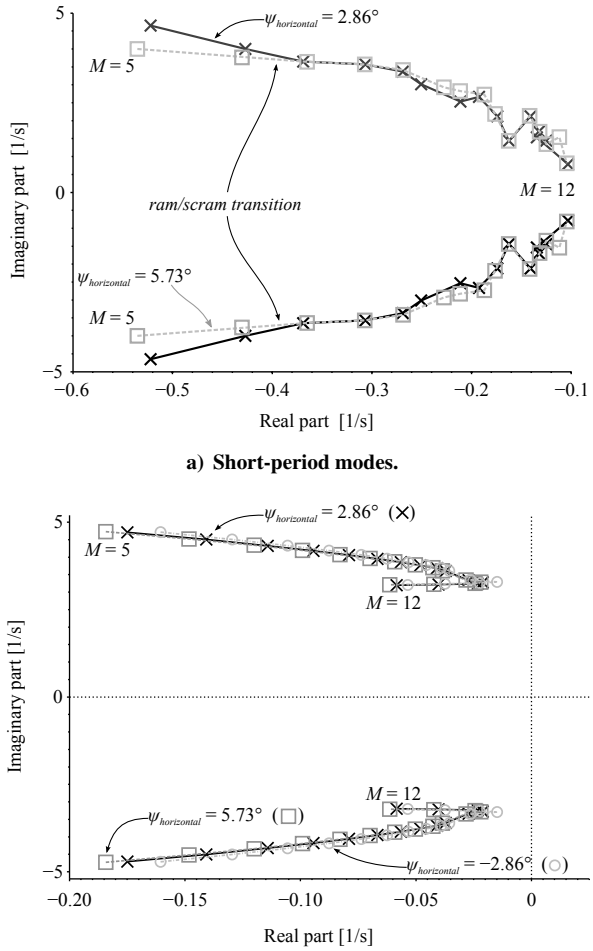

a) Short-period modes.

b) Dutch-roll modes.

Figure 10. Plot of poles of linearized dynamics for MAX-1 ($\psi_{horizontal}$ = 2.86°), an otherwise identical vehicle with twice the horizontal stabilizer dihedral angle ($\psi_{horizontal}$ = 5.83°), and a vehicle with an anhedral angle ($\psi_{horizontal}$ = −2.86°).

with a slight anhedral angle for the elevators. Furthermore, the trim variables are almost completely unchanged; an example is shown in Fig. 11. Thus the dihedral angle is an example of a design variable that can be used to alter the lateral-directional stability without much effect on any other aspect of performance.

D. Design Mach Number

The performance of the inlet has been closely tied to the flight condition or range of flight conditions it was designed [11, 14, 15, 17]. However, in each of those works, the inlet was considered in isolation from the rest of the vehicle. The MAX-1 inlet design algorithm specifies both a range of Mach numbers for which the inlet should have good performance. It does this by satisfying certain constraints on the shock locations and maximizing the pressure recovery factor at a single Mach number within that range [15].

In this work we define the range of Mach numbers as a center Mach number and a width (Mach number range) so that the bounds of the range are

$$M_{\min} = M_{design} - \frac{1}{2}M_{range} \qquad M_{\max} = M_{design} + \frac{1}{2}M_{range} \tag{18}$$

The values of M_{design} and M_{range} are given as inputs to the inlet design algorithm. As a result, the values of $M_{\min}$ and $M_{\max}$ do not necessarily correspond to performance criteria such as a specific value of pressure recovery factor.

When an inlet is operating outside its design range, various adverse effects are predicted due to strong shock interactions, and some of these have been shown to affect the overall performance of the vehicle [6].

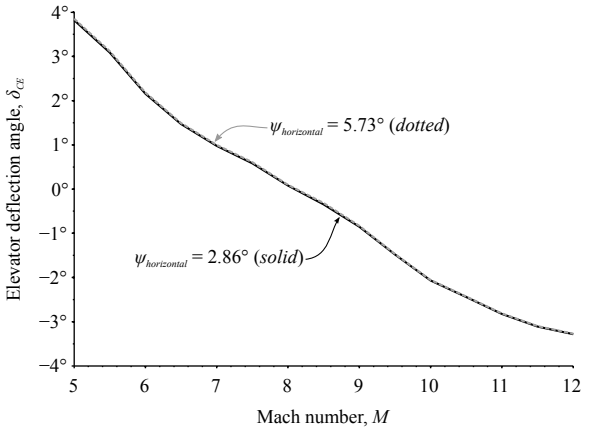

Figure 11. Plot of elevator angle (δ_{CE}) for MAX-1 ($\psi_{horizontal}$ = 2.86°), an otherwise identical vehicle with twice the horizontal stabilizer dihedral angle ($\psi_{horizontal}$ = 5.83°), and a vehicle with an anhedral angle ($\psi_{horizontal}$ = −2.86°).

However, the direct effect on fuel consumption has not been studied. In addition, there is a tradeoff between the size of the design envelope (i.e., M_{range}) and the peak performance [14]. The trajectory used here,

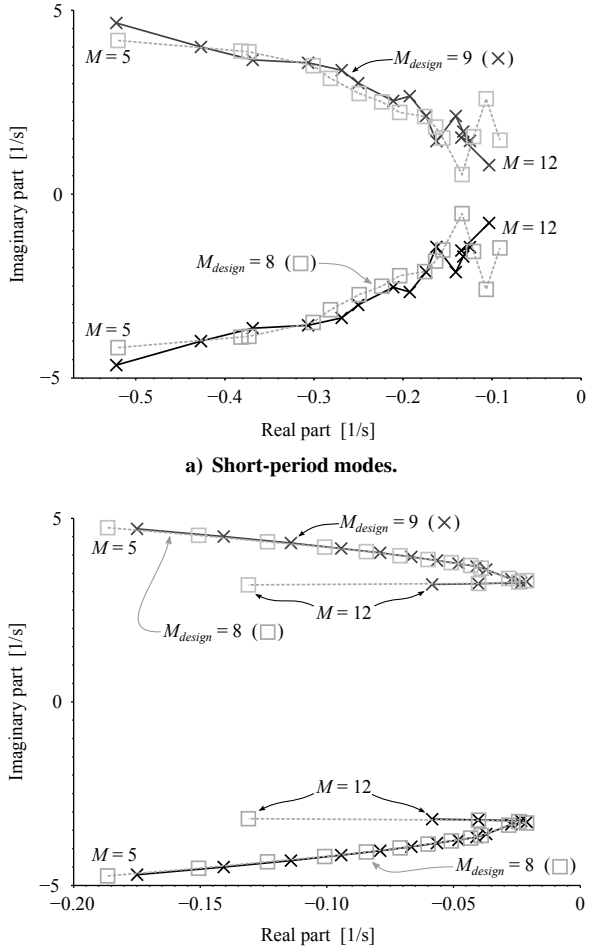

a) Short-period modes.

b) Dutch-roll modes.

Figure 12. Plot of poles of linearized dynamics for MAX-1 (M_{design}= 9) and an otherwise identical vehicle with a lower design Mach number (M_{design}= 8).

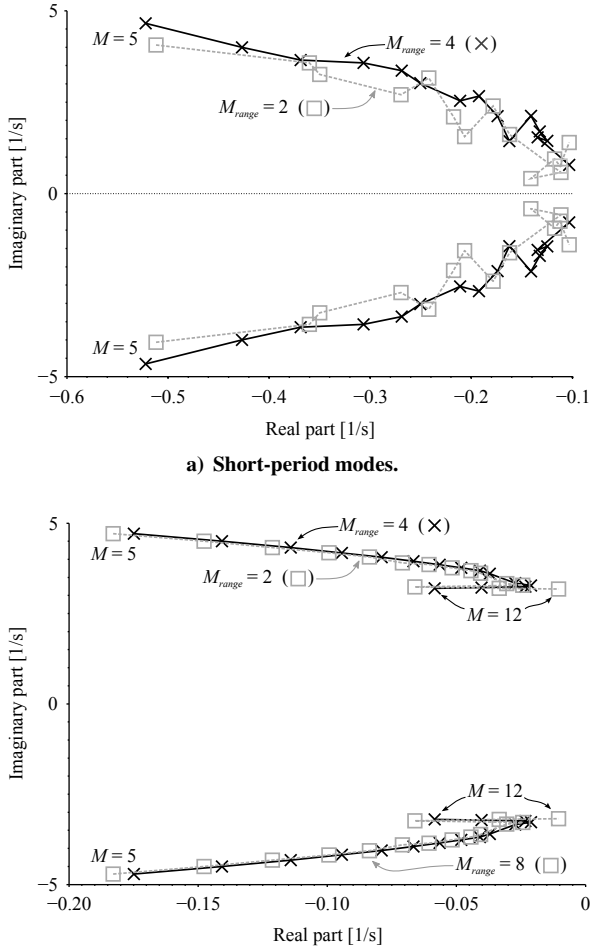

a) Short-period modes.

b) Dutch-roll modes.

Figure 13. Plot of poles of linearized dynamics for MAX-1 (M_{range}= 4) and an otherwise identical vehicle with a lower design Mach number (M_{range}= 2).

which accelerates from Mach 5 to Mach 12, has Mach numbers both below and above the MAX-1 design range of Mach 7 to Mach 11. The object of this section is to investigate how operating outside the design range affects performance and stability. In particular, it seeks to answer how wide the design envelope should be compared to the trajectory and whether the inlet should be designed for the lower Mach numbers in the trajectory range or the higher Mach numbers.

Figure 12 shows the short-period and Dutch-roll poles for MAX-1 ($M_{\min} = 7, M_{\max} = 11$) with a vehicle designed for lower Mach numbers but with the same design envelope size ($M_{\min} = 6, M_{\max} = 10$). As shown in Fig. 13a, this design change has very little effect on the short-period mode. Increasing the design Mach number appears to be slightly destabilizing for this mode, but this may be a result of the higher compression ratio that results from the way the inlets were designed. Namely, both inlets were designed to have a compression ratio (the ratio of static pressure at the end of the inlet to the freestream static pressure) of 70 at M_{design}. As a result, MAX-1 has a lower compression ratio at Mach 8 than the other design. The Dutch-roll mode, as shown in Fig. 12b, is slightly more stable for the inlet designed for higher Mach numbers.

The results shown shown in Fig. 13 compare MAX-1 to a vehicle with an inlet designed for a narrower range of Mach numbers ($M_{\min} = 8, M_{\max} = 10$). The description of these results is strikingly similar to those of the previous paragraph. The primary difference is that the poles get somewhat more chaotic at the higher Mach numbers for the inlet designed for a narrower range of conditions. This is not surprising in that the inlet has a lower upper bound for the design range than the other designs, but it is perhaps surprising that the apparent randomness is noticeable for the case where $M_{\max} = 10$ but not for the case that $M_{\max} = 11$.

The result can be explained by the fact that the inlet is also designed for a range of angles of attack as described in [15]. The inlet is specified to have continuous performance, avoiding the worst shock interactions, for a rectangular area in Mach number/angle of attack space. Since the design algorithm does this by satisfying constraints at the corners of this rectangle, the actual flight envelope might include a wider range of conditions. The sketch in Fig. 14 gives an example of how this works. In terms of shock patterns, increasing the angle of attack is similar to decreasing the Mach number, and vice versa. As a result, usually only two of the four corners of the design envelope (shown in darker gray in Fig. 14) are actively constrained. Near the other two corners, shock interactions might not occur for a range of flight conditions outside the design set. In short, the inlet design methodology specifies where shock interactions must not occur; it says nothing about the conditions for which the deleterious interactions actually do occur. Finally, the example trajectory in Fig. 14 (solid black curve) shows an example of a trajectory that goes outside the design range of conditions yet does not experience strong shock interactions. This appears to be the case for MAX-1 flying along the trajectory used in this work.

E. Inlet Compression Ratio

Apart from the design range of flight conditions discussed in the previous subsection, the other design variable is the compression ratio of the inlet. The compression ratio, r_p, is the ratio of the static pressure at the end of the inlet (or beginning of the isolator) to the freestream

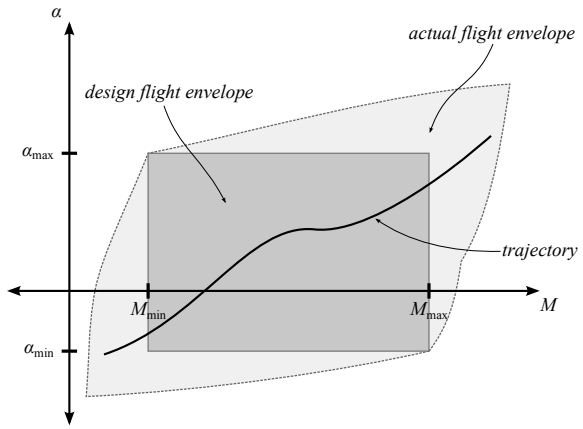

Figure 14. Sketch of a design flight envelope (darker gray) and the actual contour of flight conditions where strong shock interactions begin to occur.

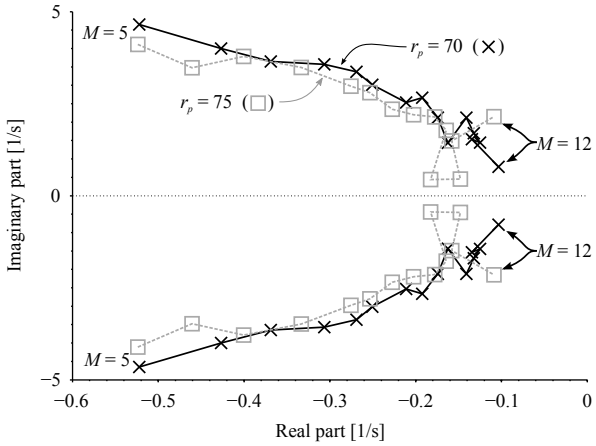

a) Short-period modes.

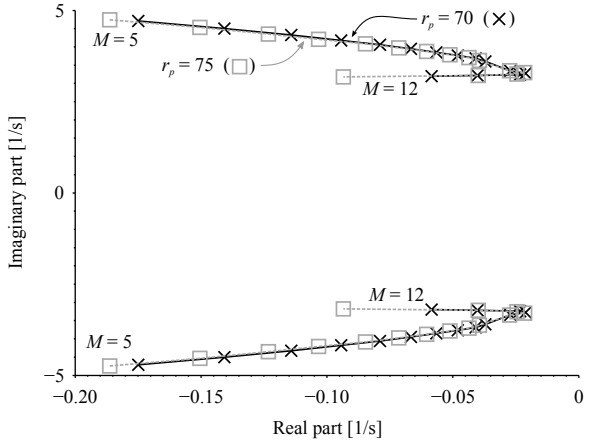

b) Dutch-roll modes.

Figure 15. Plot of poles of linearized dynamics for MAX-1 (r_p= 70) and an otherwise identical vehicle with a higher inlet compression ratio (r_p= 75).

static pressure. Altering the compression ratio was accomplished by increasing the deflection angles of each shock, and a side effect is that the height of the inlet exit decreases with a higher inlet compression ratio. A certain amount of compression is required from the inlet in order to enable combustion. The effect on combustion and thrust of increasing the inlet compression beyond the minimum level is not fully understood.

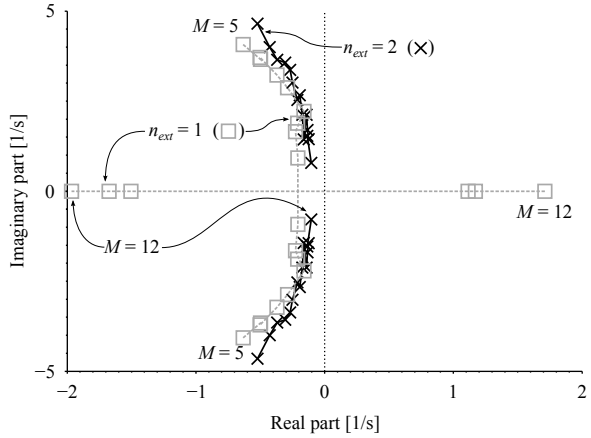

a) Short-period modes.

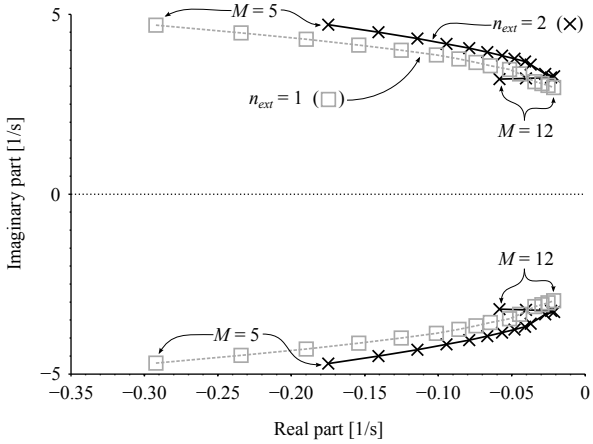

b) Dutch-roll modes.

Figure 16. Plot of poles of linearized dynamics for MAX-1 (n_{ext}= 1) and an otherwise identical vehicle with one external ramp (n_{ext}= 1).

Figure 15 shows the effect of increasing r_p on the short-period and Dutch-roll modes. The short-period mode shows relatively small and incoherent changes, and a slightly stabilizing effect for the middle flight conditions can be seen. The Dutch-roll poles in Fig. 15b show a consistently stabilizing effect from increasing r_p. The cause of this is a decrease in the trim angle of attack. The decreased angle of attack is also probably responsible for the neutral effect on the short-period mode, because the increased inlet pressure would be expected to destabilize the longitudinal dynamics. This also explains why the trim angle of attack decreases; the raised pressure on the inlet surface would tend to increase the lift coefficient, so there must be some other change to keep the lift coefficient unchanged.

F. Number of Inlet Ramps

Two design variables that have a very important effect on performance is the number of internal and external inlet ramps. The baseline MAX-1 vehicle has two external ramps (n_{ext} = 2) and two internal turns (n_{int} = 2). These variables are unique in that they are not continuous. As such changes to these design variables do not result in "sensitivities," but understanding the effects of these variables is quite important.

Figure 16 shows the short-period and Dutch-roll modes for a vehicle in which the number of external inlet shocks has been reduced to 1 (n_{ext} = 1) from the default value of 2. For MAX-1, the number of inlet shocks is also 2. It should be noted that other combinations of number of inlet shock did not result in a vehicle that could be trimmed throughout the baseline trajectory.

The stronger pressure near the nose of the vehicle for a single-external-ramp vehicle should destabilize the vehicle because it moves

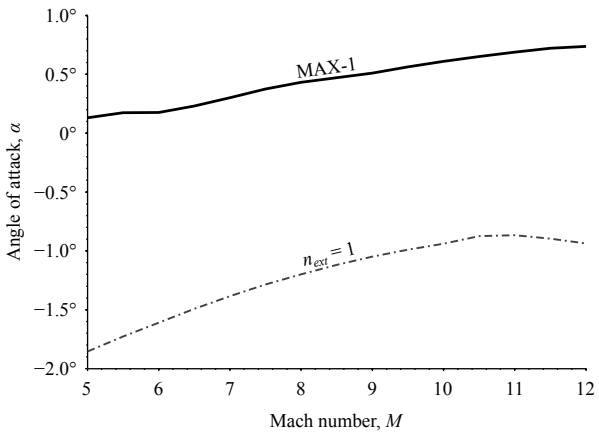

Figure 17. Plot of angle of attack (α) for MAX-1 and a vehicle with one external inlet ramp ($n_{ext} = 1$).

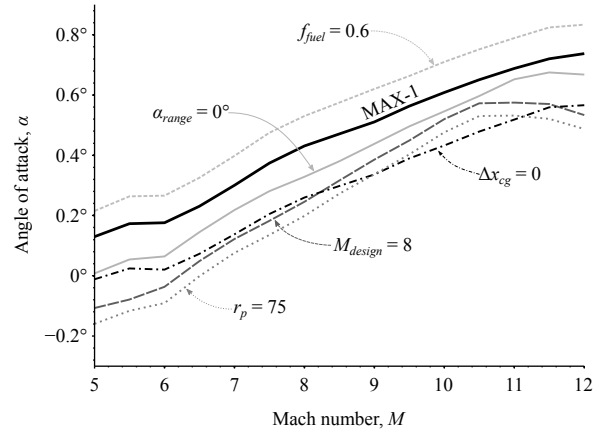

Figure 18. Plot of trim angle of attack for several vehicle designs and an accelerating trajectory.

the center of pressure forward. In Fig. 16a, it can be seen that the short-period mode becomes unstable between Mach 10.5 and Mach 11. However, the short-period modes for lower Mach numbers surprisingly increased in stability margin. The cause is probably that the dramatically lower angle of attack, as shown in Fig. 17, for the single-ramp vehicle counteracts the forward shift of the center of pressure.

G. Performance

This subsection investigates the effects of the various alterations to the design of MAX-1 on the trim variables throughout the trajectory. Six vehicle designs are compared: the baseline MAX-1 vehicle and five single-design-variable perturbations to it. These mostly match with the vehicles of the previous subsections with a few exceptions. The narrow-design-Mach number plot is not included ($M_{range} = 2$ from Sec. IV.D) because the performance is very similar to the shifted-design-Mach number values ($M_{design} = 8$ from Sec. IV.D). The design with an increased dihedral angle ($\psi_{horizontal} = 5.73°$ from Sec. IV.C) is also not shown because it has almost identical trim results to MAX-1.

Finally, an additional design with a limited range of design angle of attack is considered here. The MAX-1 vehicle has an inlet designed using

$$\alpha_{\min} = -0.5° \qquad \alpha_{\max} = +1.0°$$

so $\alpha_{range} = 1.5°$. A contrasting design with $\alpha_{\min} = \alpha_{\max} = 0°$ is considered here. The results corresponding to that vehicle are labeled $\alpha_{range} = 0°$.

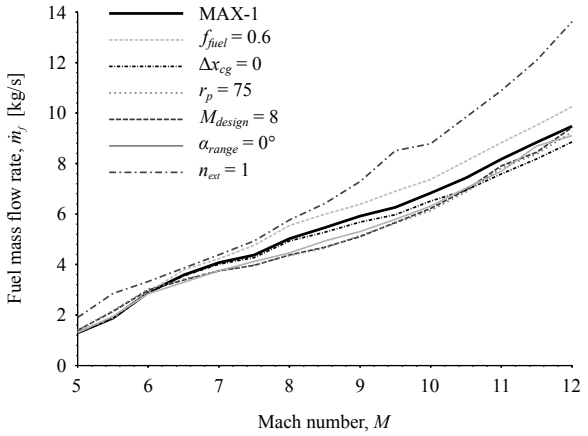

Figure 19. Plot of trim fuel mass flow rate for several vehicle designs and an accelerating trajectory.

The first of the three trim variables plotted is the angle of attack in Fig. 18. One of the most notable results is that the vehicle with an increased mass, labeled $f_{fuel} = 0.6$, has a mostly uniform increase in the angle of attack. The next feature to notice is that all of the other design alterations seem to lower the trim angle of attack. The angle of attack for the single-ramp inlet differs from that of the other vehicles and is not shown in Fig. 18. Although all of these results are explained in the previous subsections, it is somewhat surprising that increasing the mass is the only design perturbation that causes the angle of attack to increase. This is a particularly interesting result in light of the fact that reducing the angle of attack tends to also decrease drag and thus fuel consumption. A consequence of this trend is that features normally associated with poor performance, shock interactions, could indirectly cause a net decrease in fuel consumption.

Figure 19 shows the rate of fuel consumption ($\dot{m}_f$) for the various vehicle designs. All of the vehicles have similar fuel consumption for the lower Mach numbers in the trajectory. The heavier vehicle ($f_{fuel} = 0.6$) requires extra fuel compared to the other vehicles. The only exception that is the inlet designed for lower Mach numbers ($M_{design} = 8$), uses about the same amount of fuel as the heavier vehicle at Mach 6 and below. As explained before, the higher fuel consumption for the heavier vehicle comes directly from the higher trim angle of attack. The increased fuel consumption for the lower-Mach-number inlet, however, occurs despite a dramatic reduction in the trim angle of attack.

Interestingly, all of the design perturbations except for the heavier vehicle reduce the fuel consumption above Mach 6. The cause of the reduced fuel consumption of the $\alpha_{range} = 0°$ vehicle is the trade-off between the size of the design envelope and peak performance initially reported in [14]. The trajectory for the $\alpha_{range} = 0°$ vehicle shown in Fig. 18 does not have any points within the design envelope ($7 \le M \le 11$, $\alpha = 0°$), but performance is not degraded by strong shock interactions due to the phenomenon demonstrated in Fig. 14. This means at least two things about the inlet design. Since the actual high-performance envelope is much larger than the design envelope, it is difficult to know what values of $M_{\min}$, $M_{\max}$, $\alpha_{\min}$, and $\alpha_{\max}$ are most appropriate for a given trajectory. Second, it seems that some of the shock interactions that the inlet design algorithm of [15] seeks to prevent probably do not have much impact on overall vehicle performance.

The vehicle with a single-ramp inlet has the highest fuel consumption at all of the flight conditions along the trajectory. Because the bow shock at the leading edge of the vehicle must be much stronger for a single-ramp inlet, more drag and thus more fuel required is expected. The fuel increase is notable despite the sizable decrease in angle of attack, although it is possible that −2° is below the minimum-drag angle of attack.

For the remaining vehicle designs, the reduced fuel mass flow rate comes directly from the reduced angle of attack. The case with a higher

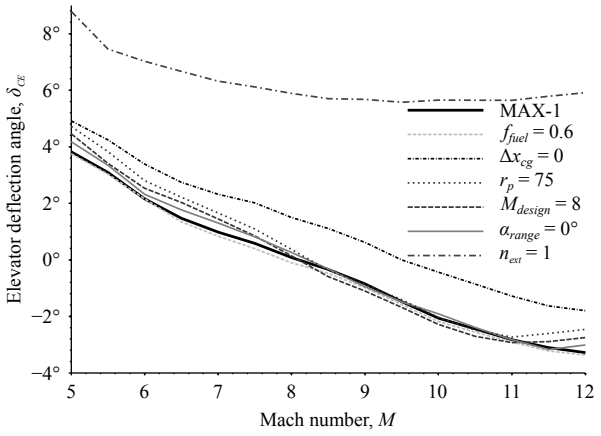

Figure 20. Plot of trim elevator deflection angle for several vehicle designs and an accelerating trajectory.

compression ratio ($r_p = 75$) may also have an effect on the combustion efficiency, but the angle of attack has a larger effect. In the case of the shifted center of gravity ($\Delta x_{cg} = 0$), this fuel savings comes at the expense of decreased stability. That strategy is somewhat problematic as Fig. 7a shows that this change in the center of gravity makes the short-period mode unstable throughout the trajectory. To make matters worse, there is a non-minimum phase zero in the longitudinal dynamics that interferes with the possibility of controlling the unstable short-period mode. Using the velocity flight path angle (γ) and the total velocity (V) as outputs, this non-minimum-phase zero results from the actions needed to increase the altitude of the vehicle. To increase altitude, the vehicle must pitch up, but to do that it must deflect the elevator trailing edges up, which decreases lift and causes a momentary decrease in altitude. At Mach 5, the short-period pole is 0.63 while the zero is at 5.49, which is plenty of separation. However, by Mach 12, the pole has moved to 3.42 while the zero is at 4.06. This indicates that a vehicle configuration in which the center of gravity shifts forward as fuel is used may be ideal. Using ballast in the nose will have this effect; as the fuel is burned and the mass of the vehicle decreases, the fixed-mass ballast will become a larger percentage of the mass of the vehicle.

In most cases, any design change that decreases the trim angle of attack both decreases fuel consumption and stabilizes the vehicle. This indicates that lighter vehicles and vehicles that get more lift from the inlet tend to have superior performance in terms of both stability and fuel consumption. However, it should be noted that this analysis has considered only a fixed trajectory with a constant acceleration. In reality, an air-breathing hypersonic vehicle would also be able to choose an acceleration at each Mach number. As a result, a change that reduces fuel consumption when the acceleration is 2 m/s^2 may result in a lower maximum acceleration in such a way that increases the fuel consumption after trajectory optimization has been performed.

The plots of elevator deflection angle (δ_{CE}) in Fig. 20 show that most of the design alterations do not have much effect on the trimmed elevator deflection angle. The two exceptions are the shifted center of gravity ($\Delta x_{cg} = 0$), which causes a change of about +2° throughout the trajectory, and the single-ramp inlet, which causes a much larger positive change. This matches expectations because the shift in position causes a direct change in the net moment about the center of gravity, and a constant shift in the elevator deflection would be expected to cancel the change in moment. Also, the single-ramp inlet moves the center of pressure forward substantially because the entire underside of the inlet experiences a high surface pressure rather than just the second half as is the case when $n_{ext} = 2$. Adding lift near the nose of the vehicle has a very significant effect on the net moment on the vehicle, so a large elevator deflection is needed to counter it. Also, this large increase in elevator deflections is a contributor to the higher fuel consumption for the single-ramp inlet vehicle.

The differences among the other vehicles in Fig. 20 are small compared to the amount the deflection angle changes throughout the trajectory. The differences that are present are probably due to the shift in the distribution of lift between the nozzle and inlet that are associated with a difference in angle of attack and interactions in the inlet. In general, anything that increases the amount of lift that comes from the inlet means a positive change in the deflection angle.

Table 2 gives a summary of the mass properties and total fuel usage of each of the vehicle designs from this section. Several of the vehicles have a slightly different mass from the baseline MAX-1 design because the correlations used by the MASTrim model to estimate the mass of a vehicle and the amount of fuel it can carry depend on the exact size of the vehicle. These deviations of less than 1% should not have a significant effect on performance, however.

The last column of Table 2 uses a measure of total-trajectory performance called rocket-equivalent specific impulse. This is the specific impulse that a rocket would need to give the same change in velocity using the same mass of fuel and oxidizer. From the rocket equation, this means that

$$\bar{I}_{sp} = \frac{\Delta V}{g \ln \frac{m_0}{m_0 - m_f}} \tag{19}$$

where g is the acceleration due to gravity on Earth's surface, m_0 is the initial mass of the vehicle, and m_f is the mass of fuel used during the trajectory. The results show that the heavier vehicle uses substantially more fuel but almost as efficiently as MAX-1 in terms of mass ratios. The most effective changes to the rocket-equivalent specific impulse were those that narrowed the range of the inlet design flight envelope ($M_{range} = 2$ and $\alpha_{range} = 0°$).

V. Conclusions

The effectiveness of design parameters such as dihedral angle to affect stability characteristics is an important aspect of hypersonic vehicle design. This work reports on both the effectiveness of design changes to alter the stability characteristics of the vehicle and the resulting effects on fuel consumption. Unsurprisingly, the most effective change for stabilizing the vehicle was found to be shifting the center of gravity forward, even when the extra mass of the ballast is neglected. However, such a shift leads to a decrease in fuel efficiency. This is because moving the center of gravity forward increases the angle of attack needed to trim the moment on the vehicle, and as a result the drag coefficient is higher. The instability in the short-period mode that is present when the center of gravity is not shifted forward is further complicated by a non-minimum-phase zero in the longitudinal dynamics.

Other changes to the design were both stabilizing and reduced fuel consumption. Among these, reducing the mass of the vehicle is a design improvement that conserves fuel for almost any air vehicle. It was shown that changes to the design that increase the lift coefficient tend to allow the vehicle to fly at a lower angle of attack. Lower angles of attack were associated with both reduced fuel consumption and increased stability.

The sensitivity analysis in this paper considered a fixed trajectory. In a multidisciplinary co-optimization of the trajectory and vehicle design, the optimizer is free to select a different acceleration for each Mach number. Thus sensitivities of the optimum acceleration to design changes would also be needed.

Although total fuel consumption is an ideal objective function for comparing the performance of several vehicles, the stability and controllability places an important constraint on the feasible design space. This work is a step toward understanding the relevant design tradeoffs required for optimization of hypersonic vehicles.

Acknowledgements

This research is funded by the Air Force Research Laboratory/Air Vehicles Directorate grant FA 8650-07-2-3744 for the Michigan/AFRL Collaborative Center in Control Sciences (Michael Bolender as technical monitor).

References

[1] Bolender, M. A. and Doman, D. B., "Nonlinear Longitudinal Dynamical Model of an Air-Breathing Hypersonic Vehicle," *Journal of Spacecraft and Rockets*, Vol. 44, No. 2, 2007, pp. 374–387.

Table 2. Table of performance parameters related to mass and fuel usage for several vehicle designs.

Vehicle	Initial mass	Initial fuel mass	Fuel used	Rocket-equivalent I_{sp}
MAX-1	30355 kg	11610 kg	5881 kg	1021 s
$f_{fuel} = 0.6$	32677 kg	13932 kg	6349 kg	1017 s
$\Delta x_{cg} = 0$	30355 kg	11610 kg	5617 kg	1074 s
$\Delta x_{cg} = 0.025$	30355 kg	11610 kg	5617 kg	1041 s
$r_p = 75$	30246 kg	11569 kg	5462 kg	1103 s
$M_{design} = 8$	30434 kg	11400 kg	5500 kg	1102 s
$M_{range} = 2$	30213 kg	11556 kg	5347 kg	1128 s
$\alpha_{range} = 0°$	30844 kg	11797 kg	5517 kg	1115 s
$\psi_{horizontal} = 5.73°$	30355 kg	11610 kg	5872 kg	1022 s
$n_{ext} = 1$	37204 kg	14230 kg	8081 kg	897 s

[2] Chavez, F. R. and Schmidt, D. K., "Analytical Aeropropulsive/Aeroelastic Hypersonic-Vehicle Model with Dynamic Analysis," *Journal of Guidance, Control, and Dynamics*, Vol. 17, No. 6, 1994, pp. 1308–1319.

[3] Frendreis, S. G. V., Skujins, T., and Cesnik, C. E. S., "Six-Degree-of-Freedom Simulation of Hypersonic Vehicles," *AIAA Atmospheric Flight Mechanics Conference*, 2009, AIAA Paper 2009-5601.

[4] Dalle, D. J., Torrez, S. M., and Driscoll, J. F., "Turn Performance of an Air-Breathing Hypersonic Vehicle," *AIAA Atmospheric Flight Mechanics Conference*, 2011.

[5] Yechout, T. R., Morris, S. L., Bossert, D. E., and Hallgren, W. F., *Introduction to Aircraft Flight Mechanics*, AIAA Education Series, Reston, VA, 2003.

[6] Dalle, D. J., Torrez, S. M., Driscoll, J. F., and Bolender, M. A., "Flight Envelope Calculation of a Hypersonic Vehicle Usinga First Principles-Derived Model," *17th AIAA International Space Planes and Hypersonic Systems and Technologies Conference*, 2011.

[7] Breitsamter, C., Cvrlje, T., Laschka, B., Heller, M., and Sachs, G., "Lateral-Directional Coupling and Unsteady Aerodynamic Effects of Hypersonic Vehicles," *Journal of Spacecraft and Rockets*, Vol. 38, No. 2, 2001, pp. 159–167.

[8] Choi, J., *Application of Hypersonic Vehicle Flying Qualities Criteria and Computation Considerations*, Master's thesis, Renssalaer Polytechnic Institute, 1992.

[9] Dickeson, J. J., Rodriguez, A., Sridharan, S., Soloway, D., Korad, A., Khatri, J., Benavides, J., Kelkar, A., and Vogel, J., "Control-Relevant Modeling, Analysis, and Design for Scramjet-Powered Hypersonic Vehicles," *16th AIAA/DLR/DGLR International Space Planes and Hypersonic Systems and Technologies Conference*, 2009, AIAA Paper 2009-7287.

[10] Dickeson, J. J., Rodriguez, A. A., Sridharan, S., and Korad, A., "Elevator Sizaing, Placement, and Control-Relevant Tradeoffs for Hypersonic Vehicles," *AIAA Guidance, Navigation, and Control Conference*, 2010, AIAA Paper 2010-8339.

[11] Dalle, D. J., Fotia, M. L., and Driscoll, J. F., "Reduced-Order Modeling of Two-Dimensional Supersonic Flows with Applications to Scramjet Inlets," *Journal of Propulsion and Power*, Vol. 26, No. 3, 2010, pp. 545–555.

[12] Torrez, S. M., Driscoll, J. F., Ihme, M., and Fotia, M. L., "Reduced Order Modeling of Turbulent Reacting Flows With Application to Scramjets," *Journal of Propulsion and Power*, Vol. 27, No. 2, March-April 2011, pp. 371–382.

[13] Dalle, D. J., Torrez, S. M., and Driscoll, J. F., "Rapid Analysis of Scramjet and Linear Plug Nozzles," *Journal of Propulsion and Power*, Vol. 28, No. 3, 2012, pp. 545–555.

[14] Torrez, S. M., Driscoll, J. F., Dalle, D. J., and Fotia, M. L., "Preliminary Design Methodology for Hypersonic Engine Flowpaths," *16th AIAA/DLR/DGLR International Space Planes and Hypersonic Systems and Technologies Conference*, 2009, AIAA Paper 2009-7289.

[15] Dalle, D. J., Torrez, S. M., and Driscoll, J. F., "Performance Analysis of Variable-Geometry Scramjet Inlets Using a Fundamental Model," *47th AIAA/ASME/SAE/ASEE Joint Propulsion Conference and Exhibit*, 2011.

[16] Anderson, J. D., *Modern Compressible Flow with Historical Perspective*, McGraw-Hill, 2002, pp. 133–142.

[17] Smart, M. K., "Optimization of Two-Dimensional Scramjet Inlets," *Journal of Aircraft*, Vol. 36, No. 2, 1999, pp. 430–433.

[18] Torrez, S. M., Dalle, D. J., and Driscoll, J. F., "A New Method for Computing Performance of Choked Reacting Flows and Ram-to-Scram Transition," *Journal of Propulsion and Power*, 2012, *submitted*.

[19] Shapiro, A. H., *Dynamics and Thermodynamics of Compressible Fluid Flow*, Ronald Press, NY, 1953.

[20] Bowcutt, K. G., "Multidisciplinary Optimization of Airbreathing Hypersonic Vehicles," *Journal of Propulsion and Power*, Vol. 17, 2001, pp. 1184–1190.

[21] Oppenheimer, M. W. and Doman, D. B., "A Hypersonic Vehicle Model Developed with Piston Theory," *AIAA Atmospheric Flight Mechanics Conference and Exhibit*, 2006.

[22] Van Driest, E. R., "The Problem of Aerodynamic Heating," *Aeronautical Engineering Review*, Vol. 15, No. 10, 1956, pp. 26–41.

[23] Chudoba, B., "Aircraft Volume and Mass Guidelines," Tech. rep., National Institute of Aerospace, June 2008, Hypersonic Educational Initiative Hypersonic Vehicle System Integration Short Course.

[24] Broyden, C. G., "A Class of Methods for Solving Nonlinear Simultaneous Equations," *Mathematics of Computation*, Vol. 19, No. 92, October 1965, pp. 577–593.

[25] "U.S. Standard Atmosphere," U.S. Government Printing Office, 1976, Washington, D.C.

[26] Durham, W., "Aircraft Dynamics & Control," http://www.aoe.vt.edu/~durham/AOE5214, accessed March 26, 2012.